PAPER

Check for updates

Conductive gradient hydrogels allow spatial control of adult stem cell fate†

Shang Song,[ade] Kelly W. McConnell, [ID][a] Dingying Shan,[a] Cheng Chen,[b] Byeongtaek Oh,[a] Jindi Sun,[d] Ada S. Y. Poon[b] and Paul M. George [ID] *[ac]

Electrical gradients are fundamental to physiological processes including cell migration, tissue formation, organ development, and response to injury and regeneration. Current electrical modulation of cells is primarily studied under a uniform electrical field. Here we demonstrate the fabrication of conductive gradient hydrogels (CGGs) that display mechanical properties and varying local electrical gradients mimicking physiological conditions. The electrically-stimulated CGGs enhanced human mesenchymal stem cell (hMSC) viability and attachment. Cells on CGGs under electrical stimulation showed a high expression of neural progenitor markers such as Nestin, GFAP, and Sox2. More importantly, CGGs showed cell differentiation toward oligodendrocyte lineage (Oligo2) in the center of the scaffold where the electric field was uniform with a greater intensity, while cells preferred neuronal lineage (NeuN) on the edge of the scaffold on a varying electric field at lower magnitude. Our data suggest that CGGs can serve as a useful platform to study the effects of electrical gradients on stem cells and potentially provide insights on developing new neural engineering applications.

1. Introduction

The microenvironment in which cells reside and interact provides complex physicochemical cues to drive dynamic cellular processes and behaviors.[1–3] By harnessing this native machinery, the use of electrical stimulation has gained tremendous interest to modulate cellular activity and restore functions for biological and clinical applications. A wide range of stimulation conditions and cell types have been explored for cell proliferation, differentiation, directed migration, calcium signaling, ion channel densities, and neurotrophic factor changes.[4–12] However, many of these studies solely focus on using a uniform electric field to probe cellular responses. It is worth noting that the variation of gradients, namely electrical gradients, directly contributes to the spatial patterning, development, and regeneration of human tissues and organs.[13–15] Therefore, studying the variation in the electrical field strength

and its cellular interaction may prove beneficial to understanding many intrinsic biological processes and create potential regenerative strategies for tissue repair.

Conductive hydrogels consist of a network matrix made of entangled polymers with electrically conductive fillers to exhibit high mechanical flexibility and electrical conductivity.[16] They are constructed in 3D structure with the ability to maintain high water content, porosity, softness, and mechanical integrity.[17,18] The physical properties of conductive hydrogels to the native tissue extracellular matrix (ECM) which is primarily composed of water and biomolecules make them the ideal candidate to mimic the natural cellular environment. In addition, conductive hydrogels can be electrically stimulated which can be highly relevant and desirable in mimicking electrical activities for neural engineering applications.[19,20] Developing new interactive conductive hydrogels that display gradual changes in electrical field strength is highly desirable to study the cellular response in a more physiological relevant manner.

In this study, we have developed conductive gradient hydrogels (CGGs) to investigate the effect of electrical gradients on neural differentiation of human mesenchymal stem cells (hMSCs). CGGs were porous and viscoelastic in nature which was ideal for cellular attachment. Importantly, they exhibited a uniform electric field in the center while displaying a varying electric field on the edge. Our results showed that applying an electrical field enhances hMSC viability and adhesion, but more importantly, the electrical field causes a distinct shift in cell differentiation. Our novel CGGs allow us not only to understand cellular behavior in a non-uniform electrical field

[a] Department of Neurology and Neurological Sciences, Stanford University, School of Medicine, 300 Pasteur Dr, MC5778 Stanford Stroke Center, Stanford, CA 94305-5778, USA. E-mail: pgeorge1@stanford.edu; Tel: +1 (650) 725-0013

[b] Department of Electrical Engineering, Stanford University, Stanford, CA, USA

[c] Stanford Stroke Center and Stanford University School of Medicine, Stanford, CA, USA

[d] Department of Biomedical Engineering, The University of Arizona, Tucson, AZ, USA

[e] Departments of Neuroscience GIDP, Materials Science and Engineering, BIO5 Institute, The University of Arizona, Tucson, AZ, USA

† Electronic supplementary information (ESI) available. See DOI: https://doi.org/10.1039/d3tb02269b

mimicking the physiological environment, but also provide a deeper understanding on electrical modulation of cell development and functions.

2. Materials and Methods

Fabrication of the gradient gel

A final 2 wt% gelatin and 10 wt% poly(ethylene glycol) diacrylate (437441, Sigma) in Phosphate Buffered Saline (PBS) were mixed for 2 hours at 65 °C. The mixture was added with 10% potassium persulfate and casted into a cylindrical mold. After the mixture solidified into a gel, it was rinsed with DI water for 5 minutes. Subsequently, it was immersed in a 33 vol% solution of Pyrrole (AC157710250, Fisher) in Ethanol for 10 minutes. This step enabled the monomers to gradually infiltrate the gel matrix, creating a gradient effect, and to polymerize into polypyrrole with potassium persulfate as the oxidant. The gel was then extracted and thoroughly washed in DI water for at least an overnight period before being used. The radial-gradient conductive gel with varying concentration of polypyrrole was formed (Fig. 1). The conductive gradient gel was cut into small disks with 3 mm in thickness and 9 mm in diameter (Fig. 1b, left). All conductive gradient disks were washed extensively and sterilized prior to use. Blank gels were formed similarly without pyrrole.

Mass balance modeling

The following assumptions were made to solve the numerical solution that described the radial diffusion of polypyrrole into the gel based on the principle of mass balance: (1) the volumetric flow rate k was constant; (2) the total gel volume remained constant; (3) the uptake of pyrrole into the gel was instantaneous, which was evidenced by the porosity change. Mass balance was described as:

$$\begin{cases} \dfrac{dM}{dt} = Q \\ Q = 2\pi(R-x) \cdot k \\ M = \pi R^2 \cdot \phi(x(t)) \\ \pi R^2 \phi = \pi(R-x)^2\phi_0 + \pi(2Rx-x^2)\phi_1 \end{cases} \quad (1)$$

with initial conditions:

$$\begin{cases} x(0) = 0 \\ x(10) = 3.5 \end{cases} \quad (2)$$

where M was the total mass of gel in the cylinder, t was time, x was the radial distance between the boundary and the edge, Q was mass flux across the front at time t, R was the radius of the cylindrical gel (4 mm), ϕ_1 and ϕ_2 were porosities for before and after polypyrrole immersion calculated based on scanning electron microscopy images (Fig. 1c), and ϕ was the average gel porosity.

Rheological characterization

Dynamic oscillatory rheology experiments were performed on a stress-controlled rheometer (AR-G2, TA instrument) using an 8-mm diameter cone-plate geometry. Disks were loaded onto the rheometer and a humidity chamber was secured in place to prevent dehydration. Frequency sweeps from 0.1–100% S^{-1} at 23 °C were performed at 5% constant strain to obtain storage moduli (G′) and loss moduli (G″) and stress relaxation was quantified under constant strain (Fig. 2).

Conductivity measurement

The conductive gradient gels were immersed and thoroughly washed in deionized (DI) water to eliminate ionic charges. They were longitudinally cut into thin slices which provided greater surface area for conductivity measurement. The experimental conductivity was measured using the direct current (d.c.) four-point probe method with a Keithley 2400 Source Meter 45 at room temperature (Fig. 3a). Physical dimensions of scaffolds were measured by a caliper. The center region diameter was 2 mm, while anything outside of the center region was considered to be the edge area up to the entire disk diameter (which is 9 mm).

Electromagnetic finite element method (FEM) simulation

Electromagnetic field computation was conducted with physical dimensions and electrical properties based on experimental conductivity as previously described[1] (Fig. 3b and c). Briefly, electromagnetic simulations were conducted on ANSYS HFSS with the finite element method (FEM) solver, which was based on the model that subdivided into many small subsections in the form of tetrahedra. A solution was found such that the interrelated fields within these tetrahedra satisfied the Maxwell's Equations across inter-element boundaries. Specifically, the electric field E is solved using the equation

$$\nabla \times \left(\frac{1}{\mu_r} \nabla \times E \right) - k_0^2 \varepsilon_r E = -j\omega\mu_0 \vec{J}_{source},$$

where $k_0^2 = \dfrac{\omega^2}{c^2}$, and ε_r, μ_r are the relative permittivity and permeability respectively. This equation makes no approximation from Maxwell's Equations, thus accurately capturing the electromagnetic field within the model. At each iterative calculation, the fields and associated S-matrix was generated, with the next iteration minimizing the field errors with an adaptive mesh refinement process. A solution was found when ΔS_{max} is smaller than the target, which is set to be 0.05% for high precision.

Cell culture

Human bone marrow derived MSCs (70022, Stemcell Technologies) were first expanded under 10% Fetal Bovine Serum (FBS) (Sigma) and 1% penicillin/streptomycin (P/S) (Fisher) in DMEM/F12 medium (Thermo Fisher Scientific). For all experiments, hMSC-seeded scaffolds were maintained under basal medium condition consisting of 2% B27 supplement (17504044, Thermo Fisher Scientific) in the neurobasal media (21103049, Thermo Fisher Scientific).
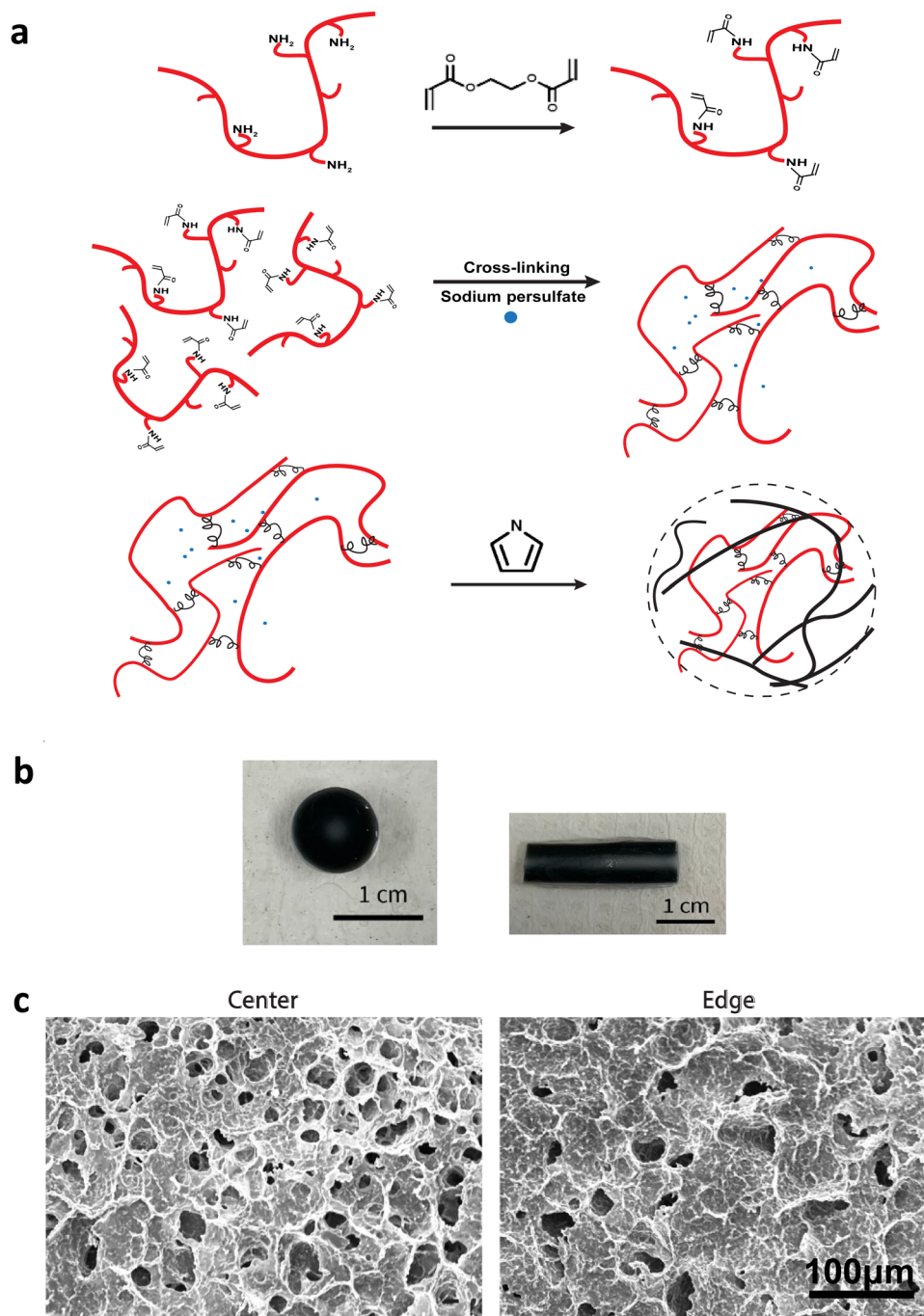
Fig. 1 Synthesis and characterization of CGGs. (a) The chemical synthesis involved crosslinking gelatin and poly(ethylene glycol) diacrylate (red strands) with potassium persulfate (black dots) in a mold to form a cylindrical gel block. The gel block was subsequently immersed into a pyrrole monomer solution which radially polymerized with residue potassium persulfate to form an extensive polypyrrole network (black strands) inside the conductive gradient hydrogel (CGG). The CGGs were further cut into individual disks (dotted lined). (b) Cross-section (left) and longitudinal (right) images of the CGG in which the amount of polypyrrole (black) was concentrated on the edge and gradually reduced in the center (white). (c) Highly magnified scanning electron microscope (SEM) images showed porous structure exhibited on the CGG surface. The porosity gradually reduced from the center to the edge (scale bar = 100 μm).

Electrically-stimulation of hMSC-seeded conductive gradient scaffolds

About 25 000 cells in medium suspension were seeded directly on top of the conductive gradient scaffolds. After the initial cell seeding, electrical stimulation (± 500 mV at 20 Hz) was applied through the conductive platform where desired electrical fields were created on the scaffold. After cell seeding on day 0, cell-seeded scaffolds were exposed to electrical fields on day 1, 3, 5 and analyzed on day 6.

Cell viability and adhesion

A viability kit (L3224, Thermo Fisher Scientific) was used per the manufacturer's protocol. The samples were incubated

1856 | J. Mater. Chem. B, 2024, 12, 1854–1863

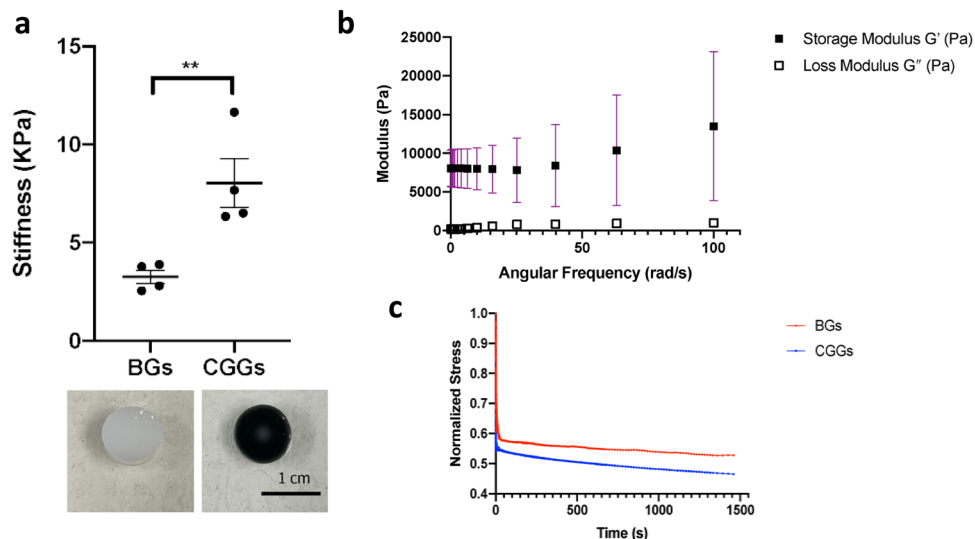This journal is © The Royal Society of Chemistry 2024

Fig. 2 Rheological properties of CGGs. (a) The stiffness of CGGs (in black) was significantly increased compared to blank hydrogels (BGs) without polypyrrole (in white) ($n = 4$, **$p < 0.01$). (b) The CGGs exhibited a higher storage modulus G' indicating their elastic behavior. (c) The stress relaxation test demonstrated the viscoelastic nature of CGGs with a higher compliance and degree of stress relaxation compared to that of BGs.

with 2 µL mL^{-1} of ethidiumhomodimer-1 and calcein AM for about 15 min at 37 °C in the dark. They were then rinsed with 1× PBS and imaged under the Keyence BZ-X710 microscope. The alive and dead cells on the conductive scaffold were quantified for viability and adhesion analysis.
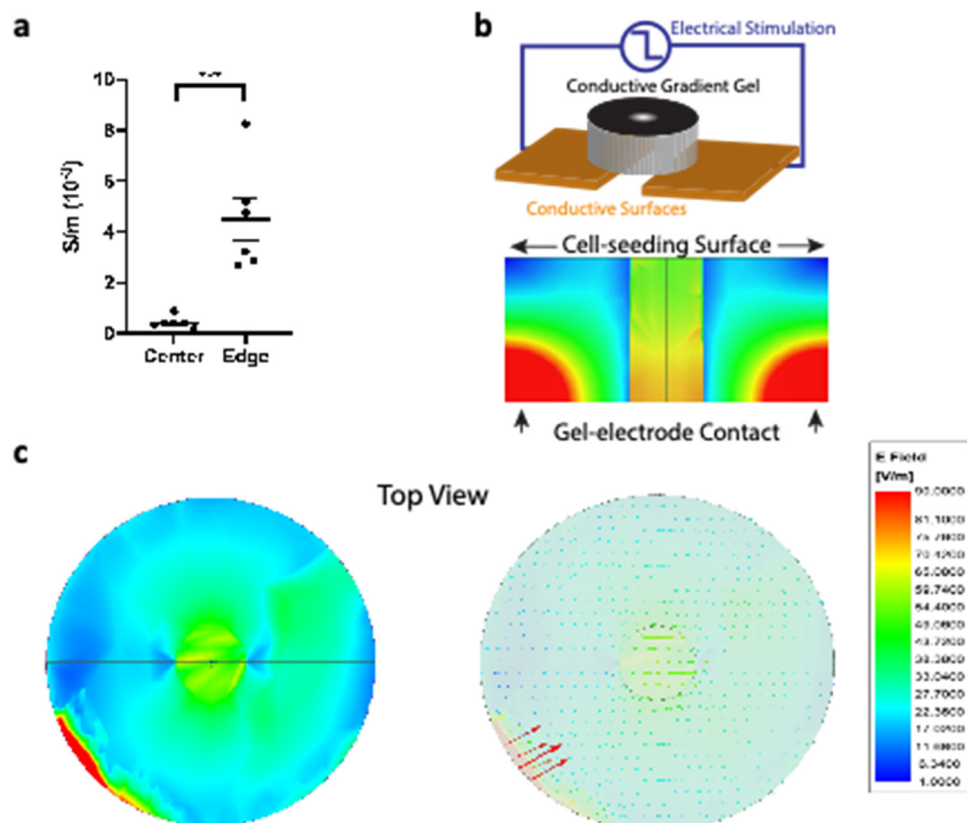

Fig. 3 Electrical characterizations of CGGs. (a) Conductivity was measured at the edge and center of CGGs. The conductivity was significantly higher at the edge compared to the center of CGGs due to increased concentration of polypyrrole ($n = 4$, ***$p < 0.001$). (b) A graphical representation of the electrically-stimulated CGG (top image). The simulated electrical field strength was computed based on experimental electrical parameters used in this study (vertical cross-section; bottom image). (c) Simulation showed both the magnitude and direction of the electrical field based on experimental parameters.

This journal is © The Royal Society of Chemistry 2024

J. Mater. Chem. B, 2024, **12**, 1854–1863 | **1857**

Immunofluorescence staining

Samples were fixed with 4% formaldehyde followed by PBS washes. They were permeabilized with 0.1% Triton X-100 for 10 min and incubated in blocking solution (PBS, 1% normal goat serum) for 30 min. They were first incubated with primary antibodies (PAX6: 42-6600, SOX1: AF3369, SOX2: AF2018, Nestin: ABD69MI from Fisher Scientific; Tuj-1: CH23005, Neuromics; NeuN: 12943S, Cell Signaling Tech.; GFAP: AB5804, EMD Millipore; Olig2: AB109186, Abcam) at a dilution of $1:100$–$1:300$ for 1 h and washed twice for 5 min with PBS to remove residues. They were then incubated with secondary antibodies (Thermo Fisher Scientific) at a dilution of $1:1000$ for 1 h, followed by PBS washes for 5 min. DAPI ($1:1000$, D9542, Sigma-Aldrich) was added for nuclear staining. Images were obtained using a Keyence BZ-X710 microscope equipped with full BZ acquisition and analysis software.

Circularity test

To find the circularity, ten random cells were chosen per sample, and the analyzer was blinded to sample condition. The Nestin and DAPI channels were separated and thresholded to isolate the cell area from the background. The circularity was measured using ImageJ, where circularity = 4pi(area/perimeter^2).

Statistical analysis

All quantifications were performed by a blinded individual. Samples were analyzed using the Student's t-test or one-way analysis of variance (ANOVA) followed by Tukey and multiple comparisons using GraphPad Prism software (San Diego, CA). A p value of < 0.05 was accepted as statistically significant for all analyses. Data are presented as mean $\pm$ SE.

3. Results and discussion

Physical and electrical characterizations of CGGs

The CGGs were made of a crosslinked network of gelatin and poly(ethylene glycol) diacrylate in which a radial distribution of polypyrrole was developed (Fig. 1a). Briefly, the pre-formed hydrogels were immersed in the pyrrole solution in which the hydrogel conductivity was achieved by post-polymerization of conductive polymer. Because pyrrole monomers diffused from the outermost to innermost of hydrogel network to polymerize in a concentration-driven and time-dependent manner, polypyrrole was formed with the highest concentration on the edge while the lowest amount in the center of the hydrogel (Fig. 1b). The porosity of hydrogel was greatly reduced on the edge compared to the center due to radial polymerization of polypyrrole (Fig. 1c). A mass balance modeling was applied to study the gel porosity. Numerical solution (eqn (1) and (2)) was obtained as an average gel porosity *versus* time immersed in polypyrrole solution in Fig. S1 (ESI†). In the beginning, the average gel porosity was equal to the initial porosity $\phi_0 = 0.1178$ based on scanning electron microscopy images (Fig. 1c). After $t = 5$ min in polypyrrole solution, the edge of blank gel was shown with radially diffused polypyrrole at a distance of $x = 1.75$ mm into the gel and the average porosity decreased to $\phi = 0.0603$ (Fig. 2b). At $t = 10$ min, the average porosity reached to a value of 0.035 (Fig. 2c), which matched the experimental observation in Fig. 1b ($x = 3.5$ mm). Based on the numerical simulation, a blank gel scaffold was expected to have fully absorbed polypyrrole at $t = 11.42$ min, where the maximum absorption would be expected ($x = R$) and the average porosity would reach its minimum value at $\phi_1 = 0.0336$.

The mechanical characterization of CGGs showed a high compliance and degree of stress relaxation. The bulk stiffness of CGGs was 8.9 ± 4.0 kPa, which was significantly higher than 3.3 ± 1.6 kPa of blank gels (BGs) without polypyrrole (Fig. 2a). The addition of polypyrrole significantly increased the bulk gel strength. The CGGs also exhibited viscoelastic behavior as shown by the higher storage modulus compared to loss modulus (Fig. 2b). The increased stress relaxation in CGGs suggests that the addition of polypyrrole contributes to the viscoelastic nature of these gels (Fig. 2b and c).

CGGs further demonstrated a conductive gradient because of differential formation of polypyrrole in the center compared to the edge of the hydrogels. The edge of CGGs showed significantly higher conductivity of $4.5 \pm 1.8 \times 10^{-3}$ S m^{-1} compared to the center $0.43 \pm 0.17 \times 10^{-3}$ S m^{-1} of CGGs (Fig. 3a). These gels were placed on a stimulating platform where electrical stimulation could be applied through conductive gel-electrode contact areas (Fig. 3b). Based on measured conductivities of CGGs, the electromagnetic finite element method (FEM) simulation showed that electric field strength was the highest at the gel-electrode contact areas and gradually decreased inside the CGGs (Fig. 3b). With a closer inspection on the cell-seeding surface of CGGs, a uniform electric field of 54–56 V m^{-1} was observed in the center compared to a varying field strength of 1–22 V m^{-1} present at the edge of CGGs when stimulating at $\pm$ 500 mV at 20 Hz (Fig. 3c). We optimized electrical stimulation parameters based on our lab's previous work. A voltage of -500 mV was determined to provide the optimal electrical field (54–56 V m^{-1}) to support optimal cell functions as demonstrated by our previous manuscripts.[4,22] A frequency of 20 Hz was chosen as it ensures stable conductivity through the hydrogel but not PBS (ionic conductivity).[19]

Cellular response on electrically-stimulated CGGs

Cells were maintained in the basal medium condition (Basal) to exclude any potential chemical effects on proliferation and induction (see Section 2. Materials and Methods). HMSCs were seeded on CGGs and received electrical stimulation on day 1, 3, and 5. Both unstimulated and stimulated conditions showed a high cell viability on day 6 at $81.3 \pm 1.02\%$ (CGG + Basal) and $83.1 \pm 1.09\%$ (CGG + Basal + ES), respectively (Fig. 4a–d and Fig. S2, ESI†). However, when comparing regionally, there was a slight enhancement in cell viability at the edge of stimulated CGGs than that of unstimulated on day 4 and 6 (Fig. 4d). Beginning on day 4, a significant reduction in the number of cells adhered on the edge of CGGs under the unstimulated condition (Fig. 4e–h). Specifically, the electrically-stimulated CGGs showed better overall cellular adhesion than the
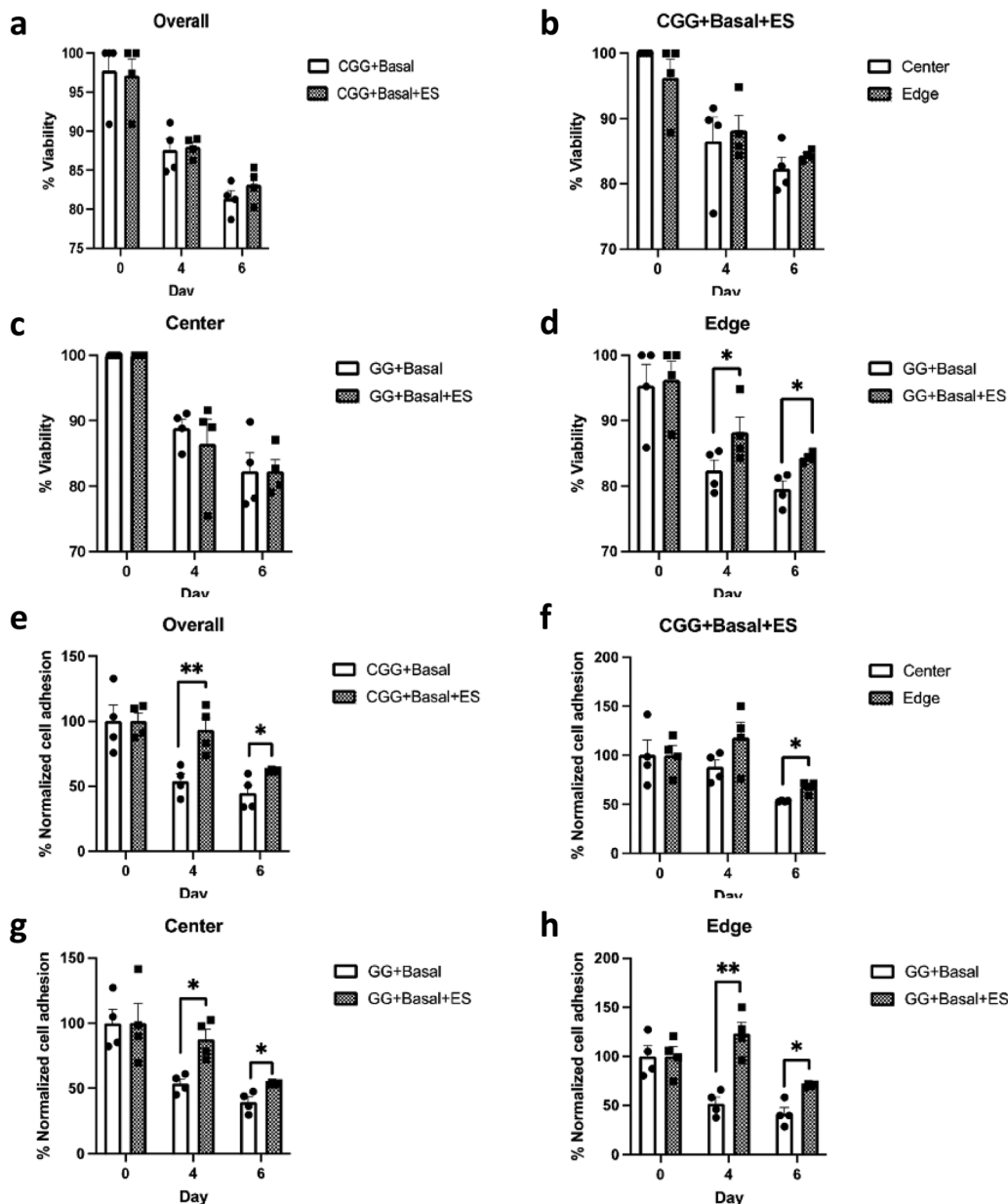
Fig. 4 Cell viability and adhesion on CGGs. (a)–(d) cell viability: Subsequent cell viability quantification showed no significant difference in cell viability on CGGs under unstimulated and stimulated conditions overall ("Overall" graph). No viability difference was observed at center and edge of the electrically-stimulated CGGs ("CGG + Basal + ES" graph). However, with respect to the center and edge of cell-seeded CGGs, a higher cell viability was observed on the edge of electrically-stimulated CGGs on later days of culture (day 4,6 from the "Edge" graph). (e)–(h) cell adhesion: A higher proportion of cells were maintained on CGGs due to electrical stimulation ("Overall" graph). This trend was observed both in the center and edge of the CGGs under the presence of electrical stimulation ("Center" & "Edge" graphs). Even within the electrically-stimulated CGGs, more cells were adhered to the CGG surface on day 6 in the edge area ("CGG + Basal + ES" graph). ($n = 4$, *$p < 0.05$, **$p < 0.01$).

unstimulated condition at $93.1 \pm 9.02\%$ and $53.9 \pm 5.59\%$ respectively on day 4 and at $61.7 \pm 0.48\%$ and $44.8 \pm 6.26\%$ respectively on day 6 (Fig. 4e). The trend showing improved cell adhesion was consistent across the center and edge of the CGGs under electrical influence (Fig. 4g–h). These data suggest that electrical stimulation significantly enhances cell attachment to CGGs without decreasing cell viability.

Electrical stimulation has shown to induce several transcription factors that are involved in cell self-renewal and survival, cell differentiation, synaptic remodeling, neural regeneration.[4–7,19,21–25] We hypothesized that the electrical stimulation and electrical gradient would influence differentiation changes and properties of the hMSCs. The unstimulated condition (CGG + Basal) showed fewer stained cells on the surface due to the lack of cellular attachment as described above (Fig. 4e and 5b). Therefore, it was statistically unreasonable to compare the stained markers between the unstimulated and stimulated groups. With a closer inspection of the stimulated condition,

we observed that hMSCs displayed a high level of neural progenitor cell markers such as Nestin, glial fibrillary acidic protein (GFAP), Sox2, and a limited amount of Sox 1 (Fig. 5 and Fig. S3, S4, ESI†). Interestingly, due to the present electrical gradient in CGGs, there was a bias in cell fate decision: oligodendrocyte transcription factor (Oligo2) was highly expressed at the center whereas NeuN was more detectable at the edge of CGGs (Fig. 5a, c and d). A uniform electrical field with greater intensity shifted hMSC differentiation toward oligodendrocyte lineage, while cells on a varying electrical field at lower magnitude preferred neuronal lineage. A cell circularity study from Nestin- and DAPI staining showed that hMSCs were more rounded on the edge than the center of CGGs (Fig. 5a, e and f). Our findings suggest that by varying electrical field, cells not only change their shapes, but also biasing cell fate toward a particular lineage which is difficult to study under a uniform electrical field.
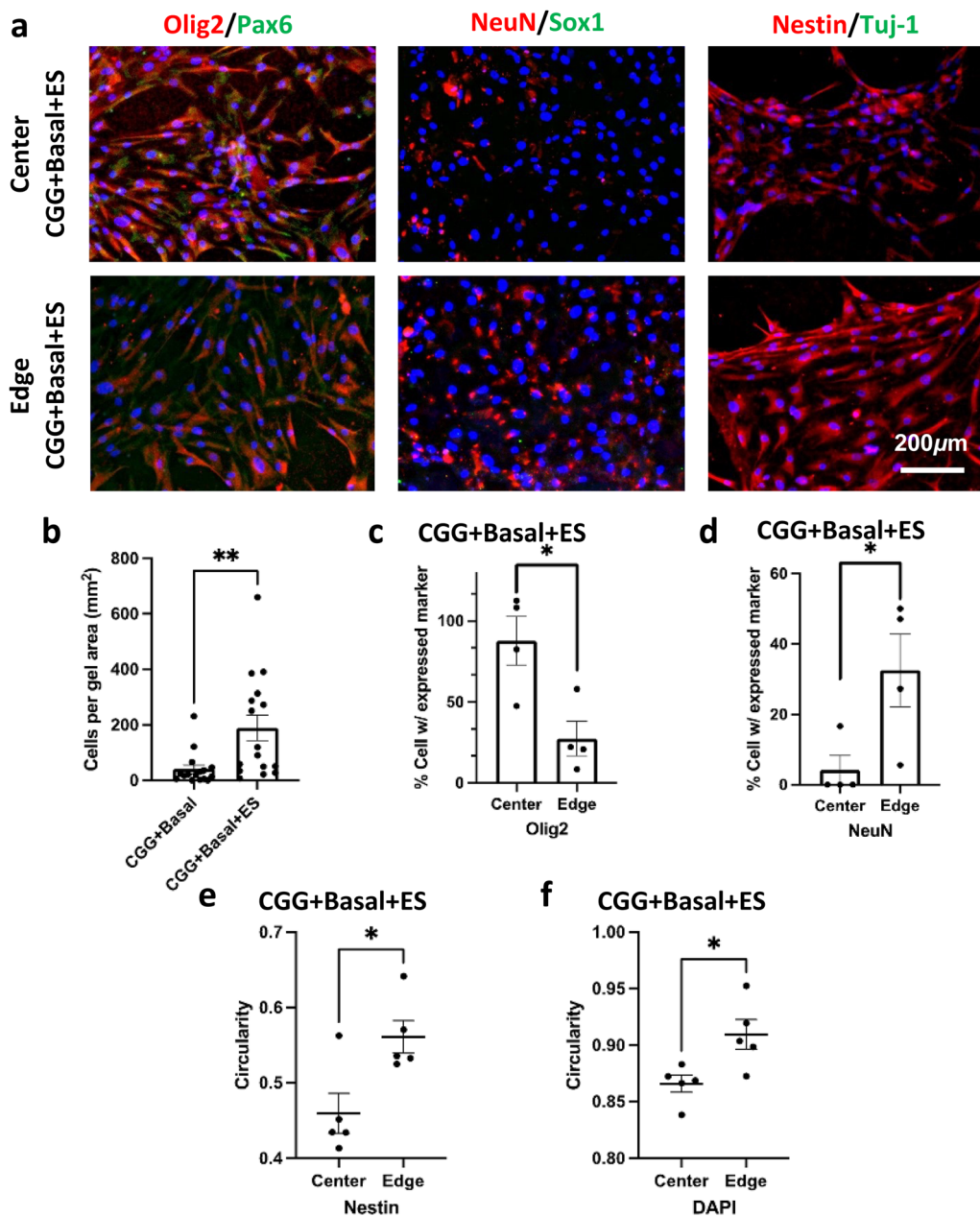

Fig. 5 Neural differentiation of hMSCs on CGGs in basal medium. (a) Stimulated hMSC-seeded CGG (CGG + Basal + ES) were immunostained with markers specifically for the neural lineage (scale bar = 200 μm). The expression of Oligo2, NeuN, and Nestin were observed in the CGG + Basal + ES group. (b) Significant cell adhesion was observed in the CGG + Basal + ES. (n = 16, **p < 0.01). (c) and (d) In the presence of electrical field, CGGs showed a greater cell expression of Olig2 in the center and NeuN in the edge of the scaffolds. (n = 4, *p < 0.05) (e) and (f). Cell circularity was quantified for Nestin- and DAPI-stained hMSCs in the center and edge of CGGs under electrical stimulation (CGG + Basal + ES). Both stains showed that cells were more rounded on the edge than the center of CGGs. (Data was represented in mean ± SEM of 10 random cells per independent sample; n = 5, *p < 0.05).

1860 | J. Mater. Chem. B, 2024, 12, 1854–1863

This journal is © The Royal Society of Chemistry 2024

3. Discussion

In this study, we created CGGs with an electrical field gradient of 54–56 V m^{-1} in the center and a varying field strength of 1–22 V m^{-1} at the edge (Fig. 3). This electrical field gradient was chosen because it mimics the electro-physiological conditions and offers electrical biases in which distinct cellular response could be studied correspondingly.[26,27] The CGGs supported hMSCs with electrical stimulation improving cellular adhesion. Stronger electric fields showed differentiation of hMSCs towards oligodendrocyte lineage while hMSCs exposed to the lower electric fields with varying strengths demonstrated neuronal markers. This new CGG allows for differentiation of multiple cell types upon a single polymeric platform to study cellular interactions and responses to non-uniform electric fields.

Electrical gradients are essential in regulating biological functions and pathophysiological diseases, such as stem cell migration along the rostral migratory stream (RMS) within the olfactory bulb,[26] embryonic development and morphogenesis,[29,30] directing nerve orientation,[30,31] wound healing,[32,33] and angiogenesis and movement of metastatic cancer cells.[34,35] The strength of endogenous electric fields in intact mammalian tissues is generally 3–5 V m^{-1} and can increase up to 10–20 V m^{-1} after injury.[28,36,37] Our previous findings have described using an unform electric field ($\sim$40–55 V m^{-1}) to promote changes in transcription factors that enhanced secretion of neurotrophic factors.[4,22] Physical disruption of cell membranes and tissues causes ionic imbalance that is suspected to act as a signal for directed cell migration and growth toward the wound until the electrical field is restored.[33,38] Injury induced electrical gradients were observed when comparing the normal cortical surface to a damaged cortex area in rat brains.[27,39,40] Aging caused the potential difference in the brain to increase from 1–1.6 mV at 5 days to 20 mV of mature rats.[27] Our conductive polymer platform creates the ability to study the effect of electrical gradients which may produce biological effects that would not be observed with uniform fields. While we have evaluated a specific stimulation paradigm based on prior work, our platform provides the opportunity to easily evaluate various waveforms and frequencies and their effect on the electrical gradient and cell function.

hMSCs shift their fates into adipogenic, myogenic, and osteogenic lineages based on surrounding ECM cues[41–43] Electrical stimulation has been commonly studied for hMSC proliferation, migration, and primarily in osteogenic differentiation. A 200 µA of direct current caused hMSC migration in the polypyrrole incorporated polycaprolactone (PCL) scaffolds due to sensing in the voltage-gated ion channels.[44] An electric field of $\sim$20 mV cm^{-1} on hMSCs enhanced expression of osteogenic differentiation markers and collagen deposition.[45] The addition of pulsed electromagnetic field (4.5 ms bursts of 20 pulses and a repetitive rate of 15 Hz) is crucial for BMP-2 dependent osteoblastic differentiation.[46] Similarly, pulsed electromagnetic field (pulse duration of 300 µs and a repetitive rate of 7.5 Hz) further increased alkaline phosphatase activity.[47] hMSCs from several tissue sources have demonstrated promising potential in neural repair such as differentiation to a particular neural lineage,[48]

formation of functional neurons,[49] and nerve regeneration after implantation.[50] A previous study reported that hMSCs adopted a neuronal-like morphology at day 10 with neural markers such as noggin, MAP2, neurofilament, β tubulin III and Nestin on 3D polypyrrole-incorporated collagen-based fibers (electrical pulses of 1.2 V with pulse duration of 5 ms at a frequency of 200 Hz).[51] A polypyrrole-alginate hydrogel, even without electrical stimulation, promoted hMSC growth and neural differentiation at 14 days (i.e. Tuj1 and MAP2).[52] Our study showed that electrical stimulation enhanced cell viability and adhesion to the CGG surface (Fig. 4). Cells seeded in the center of CGGs that created a uniform electric field with high magnitude shifted toward oligodendrocyte lineage, whereas those at the edge of CGGs preferred neuronal lineage with varying field direction with a lower field strength (Fig. 5). This suggests that electrical gradient alone could impact cell viability, shape, and preferential differentiation. Compared to previous studies, one of the advantages of our CGGs is the preferential differentiation of hMSCs on the same scaffold without using chemical induction in a short period ($<$1 week). Furthermore, aside from the impact of electrical gradients, the mechanical aspects also play a critical role in influencing neural stem cell behaviors. By modifying the base polymer properties, this can be easily explored with our new platform.

4. Conclusions

In conclusion, CGGs represent a new form of conductive hydrogels with suitable tensile strength and material compliance for electrical modulation of hMSCs. Importantly, the varying electrical gradients displayed by CGGs enables preferential hMSC differentiation toward either oligodendrocyte or neuronal lineage without using chemical induction. CGGs serve as a useful tool for studying cellular behavior and functions related to non-uniform electric fields similar to those observed in physiologic conditions. They also present a platform for examining interactions across various cell types in both healthy and diseased states in vitro. A deeper understanding of cellular responses to varying electrical gradients is pivotal for unraveling biological pathways related to endogenous tissue development and regeneration and developing new neural engineering therapeutics.

Conflicts of interest

The authors declare no competing financial interests.

Acknowledgements

This journal is © The Royal Society of Chemistry 2024

J. Mater. Chem. B, 2024, **12**, 1854–1863 | **1861**

References

1 A. Higuchi, Q. D. Ling, Y. Chang, S. T. Hsu and A. Umezawa, *Chem. Rev.*, 2013, **113**, 3297–3328.

2 F. Xing, L. Li, C. Zhou, C. Long, L. Wu, H. Lei, Q. Kong, Y. Fan, Z. Xiang and X. Zhang, *Stem Cells Int*, 2019, 2180925.

3 X. Lin, Y. Shi, Y. Cao and W. Liu, *Biomed. Mater.*, 2016, **11**, 014109.

4 S. Song, D. Amores, C. Chen, K. McConnell, B. Oh, A. Poon and P. M. George, *Sci. Rep.*, 2019, **9**, 19565.

5 B. Oh, A. Levinson, V. Lam, S. Song and P. George, *J. Vis. Exp.*, 2018, **134**, e57367.

6 S. Song and P. M. George, *Neural Regener. Res.*, 2017, **12**, 1976–1978.

7 P. M. George, T. M. Bliss, T. Hua, A. Lee, B. Oh, A. Levinson, S. Mehta, G. Sun and G. K. Steinberg, *Biomaterials*, 2017, **142**, 31–40.

8 A. Guo, B. Song, B. Reid, Y. Gu, J. V. Forrester, C. A. B. Jahoda and M. Zhao, *J. Invest. Dermatol.*, 2010, **130**, 2320–2327.

9 M. J. McKasson, L. Huang and K. R. Robinson, *Exp. Neurol.*, 2008, **211**, 585–587.

10 R. Nuccitelli, K. Lui, M. Kreis, B. Athos and P. Nuccitelli, *Biochem. Biophys. Res. Commun.*, 2013, **435**, 580–585.

11 J. G. Hardy, R. C. Sukhavasi, D. Aguilar, M. K. Villancio-Wolter, D. J. Mouser, S. A. Geissler, L. Nguy, J. K. Chow, D. L. Kaplan and C. E. Schmidt, *J. Mater. Chem. B*, 2015, **3**, 8059–8064.

12 B. Oh, Y. W. Wu, V. Swaminathan, V. Lam, J. Ding and P. M. George, *Adv. Sci.*, 2021, **8**, 2002112.

13 M. A. Lancaster, *Dev. Cell*, 2019, **48**, 1–2.

14 F. Chang and N. Minc, *Annu. Rev. Cell Dev. Biol.*, 2014, **30**, 317–336.

15 M. Levin and C. G. Stevenson, *Annu. Rev. Biomed. Eng.*, 2012, **14**, 295–323.

16 M. Tomczykowa and M. E. Plonska-Brzezinska, *Polymers*, 2019, **11**(2), 350.

17 R. A. Green, R. T. Hassarati, J. A. Goding, S. Baek, N. H. Lovell, P. J. Martens and L. A. Poole-Warren, *Macromol. Biosci.*, 2012, **12**, 494–501.

18 A. Gelmi, M. K. Ljunggren, M. Rafat and E. W. H. Jager, *J. Mater. Chem. B*, 2014, **2**, 3860–3867.

19 S. Santhanam, V. R. Feig, K. W. McConnell, S. Song, E. E. Gardner, J. J. Patel, D. Shan, Z. Bao and P. M. George, *Adv. Mater. Technol.*, 2023, 2201724.

20 V. R. Feig, S. Santhanam, K. W. McConnell, K. Liu, M. Azadian, L. G. Brunel, Z. Huang, H. Tran, P. M. George and Z. Bao, *Adv. Mater. Technol.*, 2021, **6**, 2100162.

21 S. Cohen-Cory and S. E. Fraser, *Nature*, 1995, **378**, 192–196.

22 S. Song, K. W. McConnell, D. Amores, A. Levinson, H. Vogel, M. Quarta, T. A. Rando and P. M. George, *Biomaterials*, 2021, **275**, 120982.

23 K.-A. Chang, J. W. Kim, J. A. Kim, S. Lee, S. Kim, W. H. Suh, H.-S. Kim, S. Kwon, S. J. Kim and Y.-H. Suh, *PLoS One*, 2011, **6**, e18738.

24 B. Oh, S. Santhanam, M. Azadian, V. Swaminathan, A. G. Lee, K. W. McConnell, A. Levinson, S. Song, J. J. Patel, E. E. Gardner and P. M. George, *Nat. Commun.*, 2022, **13**, 1366.

25 B. Oh and P. M. George, *Brain Res. Bull.*, 2019, **148**, 10–17.

26 S. Song, D. Amores, C. Chen, K. W. McConnell, B. Oh, A. Poon and P. M. George, *Sci. Rep.*, 2019, **9**, 19565.

27 J. Bures, *Electroencephalogr. Clin. Neurophysiol.*, 1957, **9**, 121–130.

28 L. Cao, D. Wei, B. Reid, S. Zhao, J. Pu, T. Pan, E. Yamoah and M. Zhao, *EMBO Rep.*, 2013, **14**, 184–190.

29 L. N. Borodinsky, Y. H. Belgacem, I. Swapna, O. Visina, O. A. Balashova, E. B. Sequerra, M. K. Tu, J. B. Levin, K. A. Spencer, P. A. Castro, A. M. Hamilton and S. Shim, *Dev. Neurobiol.*, 2015, **75**, 349–359.

30 L. F. Jaffe and R. Nuccitelli, *Annu. Rev. Biophys. Bioeng.*, 1977, **6**, 445–476.

31 C. D. McCaig, *J. Cell Sci.*, 1989, **93**, 723–730.

32 B. Song, M. Zhao, J. V. Forrester and C. D. McCaig, *Proc. Natl. Acad. Sci. U. S. A.*, 2002, **99**, 13577–13582.

33 M. Zhao, B. Song, J. Pu, T. Wada, B. Reid, G. Tai, F. Wang, A. Guo, P. Walczysko, Y. Gu, T. Sasaki, A. Suzuki, J. V. Forrester, H. R. Bourne, P. N. Devreotes, C. D. McCaig and J. M. Penninger, *Nature*, 2006, **442**, 457–460.

34 C.-W. Huang, J.-Y. Cheng, M.-H. Yen and T.-H. Young, *Biosens. Bioelectron.*, 2009, **24**, 3510–3516.

35 X. Yan, J. Han, Z. Zhang, J. Wang, Q. Cheng, K. Gao, Y. Ni and Y. Wang, *Bioelectromagnetics*, 2009, **30**, 29–35.

36 T. Khan, J. Myklebust, T. Swiontek, S. Sayers and M. Dauzvardis, *J. Neurotrauma*, 1994, **11**, 699–710.

37 M. L. Baer and R. J. Colello, *Neural Regener. Res.*, 2016, **11**, 861–864.

38 L. C. Kloth, *Int. J. Low Extrem. Wounds*, 2005, **4**, 23–44.

39 J. A. Hartings, F. C. Tortella and M. L. Rolli, *J. Cereb. Blood Flow Metab.*, 2006, **26**, 696–707.

40 J. A. Hartings, M. L. Rolli, X.-C. M. Lu and F. C. Tortella, *J. Neurosci.*, 2003, **23**, 11602–11610.

41 E. J. Kim, A. J. Fleischman, G. F. Muschler and S. Roy, *Biomed. Microdevices*, 2013, **15**, 385–396.

42 A. J. Engler, S. Sen, H. L. Sweeney and D. E. Discher, *Cell*, 2006, **126**, 677–689.

43 S. Song, E. J. Kim, C. S. Bahney, T. Miclau, R. Marcucio and S. Roy, *Acta Biomater.*, 2015, **18**, 100–111.

44 J. Zhang, M. Li, E.-T. Kang and K. G. Neoh, *Acta Biomater.*, 2016, **32**, 46–56.

45 M. Hronik-Tupaj, W. L. Rice, M. Cronin-Golomb, D. L. Kaplan and I. Georgakoudi, *Biomed. Eng. Online*, 2011, **10**, 9.

46 Z. Schwartz, B. J. Simon, M. A. Duran, G. Barabino, R. Chaudhri and B. D. Boyan, *J. Orthop. Res.*, 2008, **26**, 1250–1255.

47 M.-T. Tsai, W.-J. Li, R. S. Tuan and W. H. Chang, *J. Orthop. Res.*, 2009, **27**, 1169–1174.

48 X. Long, M. Olszewski, W. Huang and M. Kletzel, *Stem Cells Dev.*, 2005, **14**, 65–69.

49 L. Fu, L. Zhu, Y. Huang, T. D. Lee, S. J. Forman and C.-C. Shih, *Stem Cells Dev.*, 2008, **17**, 1109–1121.

50 E. J. Lee, L. Xu, G.-H. Kim, S. K. Kang, S.-W. Lee, S.-H. Park, S. Kim, T. H. Choi and H.-S. Kim, *Biomaterials*, 2012, **33**, 7039–7046.

51 S.-Z. Yow, T. H. Lim, E. K. F. Yim, C. T. Lim and K. W. Leong, *Polymers*, 2011, **3**, 527–544.

52 S. Yang, L. Jang, S. Kim, J. Yang, K. Yang, S.-W. Cho and J. Y. Lee, *Macromol. Biosci.*, 2016, **16**, 1653–1661.

This journal is © The Royal Society of Chemistry 2024

J. Mater. Chem. B, 2024, **12**, 1854–1863 | **1863**